Research Square

Preprints are preliminary reports that have not undergone peer review.
They should not be considered conclusive, used to inform clinical practice,
or referenced by the media as validated information.

# Strong Coupling in Bulk Nanoplasmonic Nanoplatelet Perovskite Scintillators

**Michal Makowski**

michal.makowski@port.lukasiewicz.gov.pl

Łukasiewicz Research Network - PORT Polish Center for Technology Development
https://orcid.org/0000-0001-7758-2326

**Dominik Kowal**

Łukasiewicz Research Network - PORT Polish Center for Technology Development

**Anna Pniakowska**

Łukasiewicz Research Network - PORT Polish Center for Technology Development

**Kamil Misztal**

Łukasiewicz Research Network - PORT Polish Center for Technology Development

**Mohanad Eid**

Institute of Physics, Faculty of Physics, Astronomy, and Informatics, Nicolaus Copernicus University in Torun https://orcid.org/0000-0002-5534-4084

**Joanna Cybinska**

Łukasiewicz Research Network - PORT Polish Center for Technology Development

**Winicjusz Drozdowski**

Institute of Physics, Faculty of Physics, Astronomy, and Informatics, Nicolaus Copernicus University in Torun

**Benoît Mahler**

Institut Lumière Matière

**Christophe Dujardin**

University of Lyon https://orcid.org/0000-0002-0205-9837

**Detlef Hommel**

Łukasiewicz Research Network - PORT Polish Center for Technology Development

**Liang Jie Wong**

Nanyang Technological University https://orcid.org/0000-0002-9601-9456

**Dennis Schaart**

Delft University of Technology https://orcid.org/0000-0002-3199-5608

**Sergio Brovelli**

Università degli Studi di Milano-Bicocca https://orcid.org/0000-0002-5993-855X

**Muhammad Birowosuto**

Łukasiewicz Research Network - PORT Polish Center for Technology Development
https://orcid.org/0000-0002-9997-6841

---

**Article**

**Keywords:** strong coupling, scintillators, nanoplatelets

**Posted Date:** April 10th, 2026

**DOI:** https://doi.org/10.21203/rs.3.rs-8327061/v2

**License:** This work is licensed under a Creative Commons Attribution 4.0 International License.
Read Full License

**Additional Declarations:** The authors declare no competing interests.

---

**Version of Record:** A version of this preprint was published at Advanced Materials on September 18th, 2026. See the published version at https://doi.org/10.1002/adma.75040.

# Strong Coupling in Bulk Nanoplasmonic Nanoplatelet Perovskite Scintillators

*Michal Makowski* Dominik Kowal Anna Pniakowska Kamil Misztal Mohanad Saadeldin Eid Joanna Cybinska Winicjusz Drozdowski Benoit Mahler Christophe Dujardin Detlef Hommel Liang Jie Wong Dennis Schaart Sergio Brovelli Muhammad Danang Birowosuto**

Dr. Michal Makowski, Dr. Dominik Kowal, Dr. Anna Pniakowska, Kamil Misztal, Dr. Joanna Cybinska, Prof. Detlef Hommel, Dr. Muhammad Danang Birowosuto
Address: Lukasiewicz Research Network - PORT Polish Center for Technology Development, Wroclaw, 54-066, Poland
Email Address: michal.makowski@port.lukasiewicz.gov.pl, muhammad.birowosuto@port.lukasiewicz.gov.pl
Kamil Misztal
Address: Department of Semiconductor Materials Engineering, Wrocław University of Science and Technology, Wroclaw, 50-370, Poland
Mohanad Saadeldin Eid, Prof. Winicjusz Drozdowski
Address: Institute of Physics, Faculty of Physics, Astronomy, and Informatics, Nicolaus Copernicus University in Torun, Torun, 87-100, Poland
Dr. Joanna Cybinska
Address: Faculty of Chemistry, University of Wroclaw, Wroclaw, 50-383, Poland
Dr. Benoit Mahler, Prof. Christophe Dujardin
Address: Institut Universitaire de France (IUF), 1 rue Descartes, Paris Cedex 05, 75231, France
Prof. Christophe Dujardin
Address: Universite Claude Bernard Lyon 1, Institut Lumiere Matiere UMR 5306 CNRS, 10 rue Ada Byron, Villeurbanne, 69622, France
Prof. Detlef Hommel
Address: Institute of Low Temperature and Structure Research, Polish Academy of Sciences, 50-422 Wroclaw, Poland
Prof. Liang Jie Wong
Address: CINTRA (CNRS-International-NTU-THALES Research Alliance), IRL 3288 Research Techno Plaza, 50 Nanyang Drive, Border X Block, Level 6, Singapore 637553, Singapore
Prof. Liang Jie Wong
Address: School of Electrical and Electronic Engineering, Nanyang Technological University, Singapore 639798, Singapore
Dr. Dennis Schaart
Address: Delft University of Technology, Radiation Science & Technology dept., 2629JB, Delft, The Netherlands
Dr. Dennis Schaart
Address: HollandPTC, 2629JH, Delft, The Netherlands
Prof. Sergio Brovelli
Address: Department of Physics, University of Milano-Bicocca, 20126 Milan, Italy
Prof. Sergio Brovelli
Address: INFN–Sezione di Milano-Bicocca, 20126, Milan, Italy

Keywords: *strong coupling, scintillators, nanoplatelets*

Control of light emission in solids underpins modern photonics, quantum technologies, and radiation detection. Strong coupling between excitons and confined electromagnetic modes forms hybrid light–matter states known as polaritons, enabling new regimes of emission control. To date, such effects have been largely restricted to nanoscale or ultrathin architectures and mostly reported under optical or electrical excitations, limiting their relevance for bulk scintillator applications. Here, macroscopic exciton–plasmon strong coupling is demonstrated in bulk nanocomposite scintillators based on lead-halide perovskite nanoplatelets coupled with silver nanocubes. Precise resonance alignment between excitonic and plasmonic modes is achieved through nanocube size engineering and temperature tuning, resulting in pronounced Rabi splitting and clear mode anticrossing. The extracted coupling strength exceeds both excitonic and plasmonic dissipation rates, confirming operation well within the strong-coupling regime. Angular-resolved

photoluminescence measurements directly reveal polaritonic dispersion, providing unambiguous evidence of hybrid mode formation. Strong coupling is realized in a bulk scintillating composite, demonstrating that polaritonic hybridization can be implemented directly in materials designed for ionizing radiation detection. These results establish a scalable route to polaritonic scintillators in which light yield and temporal response can be engineered through controlled light–matter hybridization, opening opportunities for next-generation radiation detectors and medical imaging technologies.

# 1 Introduction

Scintillators, materials that emit light in response to excitation by high-energy photons or particles, are indispensable for applications in medical imaging, high-energy physics detection, and nuclear instrumentation. However, conventional scintillators face persistent challenges under X-ray or $\gamma$-ray irradiation: scintillation photon extraction remains inefficient, non-radiative recombination processes dominate, and the temporal response is often too slow for advanced imaging modalities. Performance requirements differ widely across detection methods; no single metric defines a universal bottleneck. Spectral photon-counting CT prioritises high brightness and moderately fast decay, whereas high-energy physics demands radiation tolerance, high density, and minimal residual light beyond 25 ns. These contrasting constraints illustrate why traditional scintillators struggle to meet the requirements of all applications simultaneously [1, 2].

A promising route to overcome these challenges is to enhance the light–matter interaction within the scintillator medium. In the weak-coupling regime, spontaneous emission can be accelerated by the Purcell effect through engineered photonic or plasmonic environments. This concept, often termed the Purcell scintillator, has been explored using photonic crystal cavities [3, 4, 5, 6, 7, 8, 9] and plasmonic nanostructures [10, 11], which enhance radiative recombination rate and enable ultrafast luminescence [12, 13]. For applications such as TOF-PET and photon-counting CT, the relevant figures of merit differ: TOF-PET depends mainly on the arrival time of the very first photons, whereas PCCT requires sufficient timing to sustain high X-ray counting rates and enough light yield for spectral discrimination [14]. Nevertheless, sustained operation under low-dose X-ray or $\gamma$-ray exposure, as required in extended radiation imaging [15, 16] or nuclear-battery systems [17, 18], demands access to an even stronger interaction regime.

The key innovation of this work is the realization of a strong-coupling regime in a bulk material under ionizing excitation, a condition previously achieved only in thin films or in atoms confined within cavities under optical [19] or electrical [20] excitation. In this regime, the rate of coherent energy exchange between electronic excitations and the electromagnetic field surpasses the intrinsic damping of both systems. This phenomenon is described by the canonical model of two coupled oscillators exhibiting an avoided crossing, or Rabi splitting, in their eigenmodes [21]. Although strong coupling has been shown for isolated dipoles, its relevance to scintillators has remained unexplored because the emitters are dense, extended over macroscopic volumes and excited non-selectively by ionizing tracks, raising issues similar to other collective systems affected by inhomogeneous broadening and spatial averaging [21, 22]. Whether coherent light–matter interaction can survive under such conditions has therefore been unclear. We demonstrate that strong coupling occurs in a bulk scintillator and remains scalable provided three conditions are met: the emitter density supports collective coupling, the plasmonic mode volume is sufficiently small, and optical losses remain below the collective Rabi rate. The hybrid-mode eigenfrequencies are expressed as

$$\omega_{\pm} = \frac{\omega_{\mathrm{x}} + \omega_{\mathrm{c}}}{2} \pm \frac{1}{2}\sqrt{4g^2 + (\omega_{\mathrm{x}} - \omega_{\mathrm{c}})^2}\,, \tag{1}$$

where $\omega_{\mathrm{x}}$ and $\omega_{\mathrm{c}}$ denote the resonance frequencies of the emitter and the plasmonic cavity, respectively, and $g$ is the coupling strength. Strong coupling arises when $g$ exceeds the linewidths of the individual modes, leading to an energy splitting $\Delta = \omega_{\mathrm{x}} - \omega_{\mathrm{c}}$ between the emitter and cavity resonances [21, 19, 20]. In this work, we present a scintillator architecture that moves beyond the conventional weak-coupling framework by entering a regime where ionizing-radiation-generated excitations coherently interact with confined plasmonic modes. We employ caesium lead bromide ($CsPbBr_3$) nanoplatelets (NPLs), chosen

for their high photoluminescence quantum efficiency and robustness under excitation [23, 24, 25, 26], and embed silver cubic nanoparticles (Ag CNPs) within a polidimetylosiloksan (PDMS) matrix to provide tunable LSPR and strong field confinement [19, 20, 27]. A central challenge in applying strong coupling to scintillators is the apparent localization of hybrid states, since plasmonic modes are nanoscale, whereas scintillation requires modifying the response of a macroscopically distributed ensemble of dipoles. In our system this limitation is overcome because the coupling is collective: the effective coupling rate scales as $g_{\text{eff}} = \sqrt{N}\, g_0$, where $N$ is the number of coherently coupled excitons, following the canonical Dicke picture of ensemble hybridization [28, 21]. The high areal density of NPL excitons and the uniform dispersion of plasmonic cavities ensure that hybridization manifests across the full composite volume rather than at isolated hotspots. Building on our earlier demonstration of scalable plasmonic enhancement in perovskite scintillators based on nanocrystals (NCs) [11], we now use NPLs coupled to Ag CNPs of controlled side length as deterministic parameters to tune collective exciton-plasmon coupling throughout bulk materials.

By tuning the Ag CNP dimensions and the operating temperature, both the plasmon resonance and field confinement are optimized, enabling a smooth and continuous transition from weak to strong coupling [27, 29]. Under optimal conditions, we observe Rabi splitting and achieve normalized coupling ratios of $g/\omega_{\text{x}} = (0.32 \pm 0.01)$ and $(0.36 \pm 0.01)$ in photoluminescence (PL) and radioluminescence (RL) experiments, respectively. Importantly, angle-resolved PL measurements reveal a clear polaritonic dispersion and anticrossing behavior, providing direct evidence of hybrid light–matter eigenstates beyond spectral splitting alone. The observation of angular-dependent mode evolution confirms the formation of collective exciton–plasmon polaritons and excludes interpretations based solely on bimodal emitter size distribution.

To the best of our knowledge, these results represent the first experimental realization of strong coupling under ionizing radiation, providing direct evidence of coherent energy exchange between excitons in $CsPbBr_3$ NPLs and LSPR in Ag CNPs. Furthermore, quantitative analysis of the coupling strength reveals a clear route towards the ultra-strong-coupling regime, where the non-perturbative condition $g/\omega_{\text{x}} \geq 0.10$ leads to the breakdown of the rotating-wave approximation. Accessing this regime opens new opportunities for ultrafast and low-loss light–matter energy transfer, redefining the performance limits of plasmonic perovskite scintillator composites [30].

Having established both the conceptual framework and the experimental evidence for strong coupling in $CsPbBr_3$/Ag–PDMS composites, we next examine how the coupling strength can be rationally tuned through nanoscale design. The following section shows how the morphology and orientation of the emitters, together with the geometry and size of the plasmonic cubes, govern the progression from weak to strong coupling and allow precise control over exciton–plasmon hybridization.

## 2 Results

As schematically illustrated in Fig. 1, scintillation originates from high-energy processes such as electron–hole pair cascades, exciton formation, or transitions at luminescent centers, while the plasmonic mode is sustained by a nanostructured metallic cavity. When the coupling strength reaches the strong-coupling threshold, hybrid quasiparticles, polaritons, emerge. These polaritons inherit the rapid recombination dynamics of the electronic excitation and the strong optical confinement of the plasmonic cavity mode, resulting in a characteristic Rabi splitting at zero detuning ($\Omega$) corresponding to the formation of upper (UPS) and lower polariton states (LPS). Such light–matter hybridization introduces a new paradigm for scintillation, enabling ultrafast radiative pathways and reshaping the channeling of energy into the emitted field. By forming polaritonic states with a stronger photonic component and altered mode geometry, strong coupling can increase the fraction of photons that escape the material, thereby improving effective photon extraction and maintaining robust performance under continuous irradiation.

## 2.1 Tuning the coupling of the plasmonic perovskite scintillator composites

Fig. 2 provides a comparative overview of $CsPbBr_3$ emitters integrated with Ag CNPs, illustrating how the geometry of emitters (NCs versus NPLs), the side length ($a$) of CNPs, dipole orientation, and nanoscale spacing collectively determine exciton–plasmon coupling. The seven panels in Figs. 2(a–g) depict the evolution from isotropic NCs to anisotropic NPLs, showing how dimensionality, shape, and orientation redefine the local optical environment and field overlap with the plasmonic mode. In both configurations, the active perovskite phase is separated from the metallic surface by a 5 nm polyvinylpyrrolidone (PVP) shell, which suppresses non-radiative quenching while preserving strong near-field coupling, as shown in Fig. 2a. Moreover, since the flat surface of the Ag CNP hosts $(4.13 \pm 0.66)$ times more $CsPbBr_3$ emitters than spherical Ag NPs [11], the stronger near-field coupling on the flat surface enhances the average coupling strength of the $CsPbBr_3$ emitters to the Ag CNP. Replacing the NCs with ultrathin NPLs thus significantly modifies the light-matter interaction. The plate-like morphology, confirmed by transmission electron microscopy (TEM) in Fig. 2b, shows rectangular lateral dimensions of $(19.80 \pm 3.80)$ nm and $(16.03 \pm 2.74)$ nm. The NPLs also exhibit atomically flat profiles with a thickness $t$ of $(1.93 \pm 0.45)$ nm, as verified by atomic force microscopy (AFM), see Supplementary Figs. S1a-d. The smaller $t$ compared to that of NCs of $(7.03 \pm 0.20)$ nm results in a $(1.33 \pm 0.17)$-fold stronger Purcell factor for the NPLs coupled with the 100 nm Ag CNP [11]. Such atomically defined confinement also forms an effective two-dimensional excitonic system, where reduced dielectric screening and quantum-size effects enhance exciton binding energy and oscillator strength [31]. The corresponding PL spectra in Fig. 2c clearly reflect these effects. The NPL emission is centered at $(517.50 \pm 0.06)$ nm and red-shifted by $(10.03 \pm 1.03)$ nm relative to NCs, while displaying a substantially narrower linewidth. The full width at half maximum (FWHM) decreases from $(127.10 \pm 0.61)$ meV for NCs to $(104.32 \pm 0.38)$ meV for NPLs, indicating reduced inhomogeneous broadening and improved structural uniformity. This narrowing also suggests enhanced lattice coherence and diminished phonon-assisted broadening, consistent with the formation of a more monodisperse excitonic ensemble. The spectral narrowing corresponds to a longer optical dephasing time, increasing from $(10.36 \pm 0.05)$ fs to $(12.62 \pm 0.05)$ fs, signifying improved temporal coherence of the excitonic transition [25, 31]. The resulting sharper excitonic resonance provides a more distinct spectral channel for hybridization with the plasmonic mode [21, 19].

The conceptual illustration in Fig. 2d highlights two intrinsic advantages of the NPL geometry. First, the pronounced Stokes shift of NPLs, as also shown in Supplementary Fig. S2a effectively separates absorption and emission bands, mitigating self-absorption and enabling deeper optical penetration in bulk composites. Second, angular-resolved PL measurements, as shown in Supplementary Fig. S2b confirm that the transition dipole moments of NPLs are confined within the NPL plane, whereas NCs exhibit isotropic dipole orientation. This pronounced in-plane alignment ensures optimal overlap with the plasmonic cavity field, which is predominantly polarized parallel to the metal surface [32]. Consequently, NPLs couple more efficiently to the plasmonic near field, supporting stronger radiative channels and directional photon emission, both essential for achieving the strong-coupling regime [32]. In this configuration, even minor variations in emitter orientation or spacing induce significant changes in coupling efficiency, underscoring the importance of geometric precision in attaining reproducible plasmon–exciton hybridization. Thus, the NPL configuration unites higher oscillator strength, improved field alignment, and reduced emitter–metal separation, three cooperative factors that collectively strengthen exciton–plasmon hybridization.

Spectral tunability of the plasmonic component was examined by systematically varying $a$ of the Ag CNPs as seen in Fig. 2e. The values of $a$ are $(84.25 \pm 2.33)$, $(80.64 \pm 2.83)$, and $(76.19 \pm 1.85)$ nm and later we attribute them to 85, 80, and 75 nm, respectively [29, 27]. Reducing $a$ from 85 to 75 nm induces a distinct blueshift of the LSPR by $(93.04 \pm 4.34)$ meV accompanied by a reduction of the FWHM by $(67.89 \pm 2.18)$ meV, see Supplementary Fig. S3. The resonance shift follows the expected $1/a$ dependence of the dipolar LSPR energy, confirming that geometric scaling alone allows precise control of exciton–plasmon detuning [27, 29, 33]. This systematic dependence demonstrates that the plasmonic resonance can be finely tuned through lithographic or colloidal synthesis parameters,

providing a deterministic route for energy alignment with excitonic transitions.
Complementary temperature-dependent behavior further enhances this tunability, see Fig. 2f. Upon cooling from 300 K to 10 K, the LSPR experiences an additional blueshift of (60.03 ± 35.48) meV accompanied by a reduction of the FWHM by a factor of (2.67 ± 1.16), as shown in Supplementary Fig. S4, attributed to reduced electron–phonon scattering and contraction of the dielectric function of silver [34]. In contrast, the NPL emission red-shifts by (20.21 ± 10.94) meV owing to band-gap renormalization and exciton localization in $CsPbBr_3$ [35]. These simultaneous but opposite shifts enable dynamic control of exciton–plasmon detuning without structural modification, introducing a temperature-tunable coupling parameter. Together, size and temperature adjustments enable bidirectional detuning control, providing a continuous and reversible pathway between weak and strong coupling.
To visualize the spatial distribution of plasmonic fields, finite-difference time-domain (FDTD) simulations were performed, and the intensity distribution is shown in Fig. 2g. The calculated intensity maps reveal four pronounced $|E|$-field maxima at the cube corners, consistent with the near-field hotspots characteristic of dipolar cube modes. These regions correspond to where NPLs, if positioned nearby, experience the strongest plasmonic coupling. The near-field distribution confirms intense localization at the cube corners, supporting nanometric optical confinement suitable for enhanced exciton–plasmon interaction and potential polariton formation.
The combined structural, spectroscopic, and theoretical analyses in Figs. 2(a–g) establish a comprehensive framework linking the nanoscale morphology of $CsPbBr_3$ NPLs to their improved optical coherence and coupling efficiency. By rationally tuning particle size, temperature, and emitter geometry, the system enables deterministic control of exciton–plasmon detuning, providing a robust physical basis for the macroscopic composites discussed below. Together, these results demonstrate a controllable pathway for engineering light–matter hybridization in bulk plasmonic scintillators, bridging nanoscale photonics with macroscopic radiation detection.
Figs. 2(h–k) present the macroscopic realization of the $CsPbBr_3$/Ag–PDMS composites required for scintillation applications. Scintillators must ultimately be manufactured as centimeter-scale pieces, and any nanophotonic concept must therefore demonstrate its ability to scale beyond thin films. Here, $CsPbBr_3$ NPLs and Ag CNPs are uniformly dispersed in transparent PDMS matrix with a diameter of (1.53 ± 0.09) cm and a thickness of (0.48 ± 0.04) cm. The PDMS host preserves optical clarity and structural stability, preventing nanostructure degradation during curing. Composites prepared with Ag CNPs of $a$ between 75 and 85 nm, together with the reference sample, show a gradual color shift from bright green to metallic hues, consistent with tunable plasmonic resonances. High transparency and efficient photon outcoupling are maintained even at 5 wt% Ag loading, confirming the scalability of this architecture towards radiation-hard scintillators with engineered light–matter interactions. The overall mass density, however, remains essentially that of the PDMS host: Sylgard 184 has a density of about 0.97 $g/cm^{-3}$, and the combined loading of $CsPbBr_3$ nanoplatelets and Ag nanocubes is sufficiently low to alter it only marginally.

## 2.2 Polariton spectral splitting probed by radioluminescence

Building upon the structural and optical framework established above, we next examined the hybridization between excitonic and plasmonic modes under ionizing-radiation excitation. The light–matter interaction was probed not only by PL but also by RL, as previously demonstrated to be feasible in our earlier work [11]. In that study, using 100 nm Ag CNPs, a possible mode crossing was observed at zero detuning between the emission and the plasmonic resonance at (10 ± 2) K (the lowest achievable temperature), accompanied by a Purcell enhancement of (6.25 ± 0.36) [11]. To complement the experimental results, the coupling dynamics were modeled using the Jaynes–Cummings (JC) Hamiltonian. The simulated temporal correlation functions and corresponding spectra, as shown in Supplementary Figs. S5a-f illustrate the evolution of coherent oscillations and mode splitting as a function of coupling strength $g$. The simulated behavior reproduces the characteristic anti-crossing and damping trends, confirming that the experimental parameters for all Ag-CNP-doped samples fall within the strong-coupling regime.

Here, temperature-dependent RL spectra were recorded for $CsPbBr_3$/Ag–PDMS composites containing Ag CNPs with $a$ of 85-, 80-, and 75-nm, together with a $CsPbBr_3$–PDMS reference sample. Our aim was to increase the zero-detuning temperature ($T_0$), corresponding to either the mode crossing (weak coupling) or anti-crossing (strong coupling), by reducing the nanoparticle size. This is expected because smaller Ag CNPs exhibit blue-shifted plasmonic resonances. The scattering spectra confirm blue shifts of (17.21 ± 3.02), (74.11 ± 5.32), and (138.89 ± 6.34) meV for the 85-, 80-, and 75-nm Ag CNPs, respectively, relative to the 100 nm Ag CNPs (Fig. 2).

The resulting RL spectral maps in Figs. 3a and 3b show two well-resolved emission branches for the 85- and 80-nm samples, separated by a pronounced energy gap that persists across the measured temperature range. These features, absent in both the 75 nm composite and the $CsPbBr_3$–PDMS reference, confirm the formation of hybrid exciton–plasmon polaritons only when the coupling strength exceeds the combined damping of the excitonic and plasmonic modes. In the RL spectra of 85 nm sample of Fig. 3a, the detuning $\Delta = \omega_x - \omega_c$, see Eq. 1, is (-6.05 ± 2.05) meV at 10 K, increasing to (74.17 ± 3.48) meV at 300 K. Theoretical modeling based on the temperature-dependent shifts of the bare excitonic ($\omega_x$) and plasmonic ($\omega_c$) modes predicts $T_0$ at (31.75 ± 4.89) K. The bare $\omega_x$ and $\omega_c$ modes, determined independently, do not coincide with the hybrid energies observed in emission, which already reflect exciton–plasmon mixing. However, the experimental spectra indicate that the apparent zero-detuning point $T_0^{exp}$ occurs near (110 ± 10) K, where the theoretical detuning is (21.59 ± 3.16) meV. This shift reflects the influence of linewidth asymmetry and mode hybridization, which displace the observable resonance from the ideal crossing condition [36].

Reducing the cube size to 80 nm shifts the detuning evolution, with $\Delta$ changing from (-61.04 ± 4.20) meV at 10 K to (18.97 ± 3.85) meV at 300 K. The bare-mode model places $T_0$ near (230 ± 10) K, whereas the observed resonance appears at $T_0^{exp}$ of (140 ± 10) K, where $\Delta$ = (-33.41 ± 3.28) meV. The faint intermediate band visible near the center of Fig. 3b originates from uncoupled excitonic emission, most likely from localized exciton states that do not participate in plasmonic coupling, consistent with the known multiexciton generation in $CsPbBr_3$ NPLs [37].

In contrast, the RL spectra for the 75 nm CNPs in Fig. 3c show a single, unsplit emission band centered at (2.42 ± 0.01) eV, closely resembling that of the uncoupled emitter in Fig. 3d. At room temperature, the emission peak exhibits a (10.03 ± 3.98) meV blue shift relative to the reference sample, and, similarly to the bare $CsPbBr_3$–PDMS composite, it red-shifts by (20.03 ± 0.66) meV upon cooling to 10 K. This behavior confirms the absence of mode hybridization and indicates a transition back to the weak-coupling regime.

The observed avoided crossing for 85 and 80 nm Ag CNPs mirrors the detuning evolution predicted by the Jaynes–Cummings model [38, 21] and represents a direct manifestation of coherent hybridization. In temperature-dependent PL spectra of the same composites, as shown in Supplementary Fig. S6, the two polariton branches are clearly resolved at low temperature but gradually merge into a single emission band as phonon-driven dephasing broadens the excitonic linewidth. This behavior is consistent with the expected suppression of coherent exchange under optical excitation [39, 40, 41, 21]. Under ionising excitation, however, the radioluminescence spectra retain a well-defined Rabi doublet over the same temperature range, indicating that polaritonic relaxation pathways remain operative even when PL-derived signatures collapse. The corresponding unnormalized RL and PL maps are presented in Supplementary Figs. S7 and S8.

To further verify that the observed spectral splitting originates from coherent exciton–plasmon hybridization rather than from a bimodal distribution of emitters, angle-resolved PL measurements 80 nm Ag CNPs composite were performed at 80K, and the results are presented in Fig. 4. In a scenario involving two spectrally distinct but uncoupled excitonic populations, the emission energies would remain angle-independent, and no avoided crossing would be observed [42]. The observed peak-to-peak splitting decreases by (30 ± 10)% upon changing the excitation wavelength; this reduction arises from a modification of the effective exciton energy and detuning under different excitation conditions rather than from a change in the intrinsic coupling strength. Minor variations may additionally reflect local spatial heterogeneity of the composite and differences in the probed excitation region. Nevertheless, the

extracted peak positions exhibit a clear anticrossing and dispersive LPS and UPS consistent with the coupled-oscillator model described by Eq. 1 [43]. The angular evolution is quantitatively reproduced using the same coupling parameters obtained from the temperature-dependent analysis, confirming that the doublet arises from strong light–matter coupling rather than from spectral heterogeneity of the nanoplatelet ensemble.

## 2.3 Splitting analysis

The temperature-dependent dispersions extracted from the RL spectra allow a quantitative reconstruction of the interaction parameters governing the hybrid exciton–plasmon states. Fig. 5 overlays the fitted UPS and LPS branches with the independently determined bare exciton ($\omega_x$) and plasmon ($\omega_c$) energies, providing a direct comparison between the measured hybrid energies and the underlying uncoupled resonances. This representation highlights the characteristic anticrossing of the polariton branches, enabling a quantitative reconstruction of the coupling regime.

To determine the coherent coupling rate, we analyze the spectral splitting using the detuning and linewidth parameters extracted from temperature-resolved RL and PL spectra (Figs. S3–S4 and S9–S10). The coupling strength $g$ is obtained from the observed mode separation $\Delta\omega_{\mathrm{obs}}$ through

$$g = \frac{1}{2}\sqrt{\Delta\omega_{\mathrm{obs}}^2 - \Delta^2 + \frac{(\kappa-\gamma)^2}{4}} \tag{2}$$

which accounts for both the energy detuning $\Delta = \omega_x - \omega_c$ and the damping rates of the plasmonic ($\kappa$) and excitonic ($\gamma$) modes. Strong coupling is achieved when $g > (\kappa+\gamma)/4$ and the cooperativity parameter exceeds unity [21, 30, 44]. All evaluated quantities are summarized in Supplementary Tables S1 and S2.

For the 85 nm nanocubes, the coupling rate is $g_{85} = (89.88 \pm 6.21)$ meV, exceeding the threshold $(((\kappa+\gamma)/4)_{85})$ of $(77.84 \pm 5.64)$ meV and yielding a cooperativity of $(2.39 \pm 0.08)$ (Fig. 5a). The 80 nm cubes exhibit a comparable interaction strength ($g_{80}$) of $(97.86 \pm 7.19)$ meV relative to a threshold $(((\kappa+\gamma)/4)_{80})$ of $(74.09 \pm 3.99)$ meV, with a cooperativity of $(2.65 \pm 0.09)$ (Fig. 5b). Typical plasmon–exciton platforms exhibit coupling strengths in the 50–150 meV range, as summarized in recent reviews of strong and ultrastrong light–matter interaction [21, 30]. The values of $g \approx 90$ meV obtained here therefore fall squarely within the expected scale for plasmonic nanocavities. In both geometries, the hybrid branches remain distinctly separated across the accessible detuning range, indicating that coherent exchange dominates over dissipative processes even at elevated temperatures.

The temperature dependence of the hybrid energies (Fig. 5a and b) also reveals the origin of the minimum splitting. Because the exciton and plasmon exhibit markedly different intrinsic thermal dispersions, the temperatures at which their uncoupled modes intersect differ substantially from the temperatures that minimize the hybrid separation ($T_0^{exp}$). It makes the difference between experimentally obtained $T_0^{exp}$ and those extracted from the theory $T_0^{theory}$. For the 85 nm cubes, these occur at $T_0^{theory,85}$ = $(31.74 \pm 0.21)$ K and $T_0^{exp,85}$ = $(110.32 \pm 1.64)$ K, respectively, while for the 80 nm cubes the corresponding values are $T_0^{theory,80}$ = $(231.19 \pm 1.74)$ K and $T_0^{exp,80}$ = $(130.15 \pm 2.85)$ K. This distinction reflects the fact that RL spectra probe the already-hybridized eigenstates rather than the bare resonances.

Finally, Fig. 5c illustrates the geometric dependence of the coupling rate. The extracted $g$ decreases with increasing Ag CNPs side length, consistent with reduced field confinement in larger plasmonic cavities [27]. The experimental values lie within the theoretical bounds calculated for low- and high-fluence excitation (Supporting Information, Section *Exciton–plasmon coupling rate*) [45]. While tuning the $a$ of Ag CNP from 75 to 90 nm, the theoretical $g$ falls in between 16.61 and 241.79 meV range (as shown in the dashed area of Fig. 5c). Both $g_{\mathrm{PL}}$ and $g_{\mathrm{RL}}$ obtained from the experiments fall in the middle of the theoretical $g$. The consistency between the model and the measurements reinforces the validity of the extracted parameters and demonstrates that the hybridization strength can be rationally tuned through nanoscale geometry.

## 3 Conclusion

We have demonstrated that macroscopic perovskite scintillators can operate in the strong light–matter coupling regime, a condition previously limited to nanoscale optical cavities. By integrating $CsPbBr_3$ NPLs with Ag NCs and engineering their geometry and temperature, we deterministically tune exciton–plasmon detuning and observe clear Rabi splitting for both RL and PL measurements. The extracted coupling strengths exceed the combined dissipative losses, confirming the formation of coherent upper and lower polariton branches in a bulk composite system.

The strong hybridization arises from the intense plasmonic confinement at the NC corners together with the in-plane dipole alignment and large oscillator strength of the NPLs. These polaritonic states remain robust even under ionizing radiation, as evidenced by RL spectra and emission-dynamics measurements that reveal polariton-governed relaxation pathways. This establishes strong coupling as an active degree of freedom for controlling scintillation behavior, complementing and extending traditional Purcell-based or materials-chemistry approaches.

Overall, our results introduce a new design paradigm in which scintillator performance is shaped through polaritonic dispersion in addition to electronic structure. This approach enables engineered decay pathways, enhanced extraction, and tunable radiative behavior in scalable bulk architectures. Plasmonic perovskite scintillators, therefore, emerge as a versatile platform for polariton-enabled radiation detection, bridging concepts from nanophotonics with high-energy physics and medical imaging technology.

## 4 Experimental Section

*Numerical Simulations*:

A FDTD model of an Ag CNP is made in Ansys Lumerical software using the literature data [46] for the dielectric function of Ag and refinement for the CNP form. For this purpose, the literature data is initially fitted with the Drude-Lorentz (including 3 Lorentz terms) model in the 1.50 - 4.15 eV range, and the damping factors in the plasma part and the Lorentz parts are then tuned to best match the simulated scattering spectra with the experimental spectra provided by the manufacturer. To simulate low temperature behaviour of CNP, the plasma damping factor is then decreased 10 times, and the Lorentz damping factors are decreased by 10 % [47]. Corners and edges of the CNP are rounded with a 2 nm radius, and a 5 nm outer shell made of PVP is added. An in-plane point dipole source centred at the cube face, 6 nm from the Ag interface, is used to simulate the plasmonic mode. A total-field scattered-field source is used to simulate the scattering spectra. A conformal mesh was used throughout the simulation, with 2 nm refinement in the Ag CNP body and 0.5 nm refinement in the edge and corner zones.

*Sample preparation*:

To ensure the highest possible quality and reproducibility of our results, $CsPbBr_3$ NPLs and monodispersive Ag CNPs were obtained from Quantum Solutions and Nanocomposix, respectively. Four vials were prepared, with 1g of Sylgard 184 Silicone Elastomer PDMS. Each vial was supplied with 0.02 weight percent $CsPbBr_3$ NPLs in PDMS monomer. One solution was left unchanged, while the other three were supplemented with Nanocomposix Ag CNPs. To maintain an accurate NPL-to-CNP ratio, the samples were doped with precisely adjusted amounts of CNP solutions equal to 62, 58, and 55 mg for 85, 80, and 75 nm Ag CNPs, respectively. These solutions were carefully processed to promote NC attachment to the NP [27]. Samples were placed in the vacuum furnace at 80$^o$C for 3h to ensure complete solvent evaporation. Afterwards, 0.1 g of PDMS curing agent was injected into each vial, and the mixture was carefully mixed. To maintain an even distribution of NPLs and CNPs throughout the composite, samples were cured in an oil bath at 150$^o$C for 15 minutes. After curing, the samples were removed from the mould, resulting in smooth surfaces.

*RL measurements*:

The RL measurements were performed using a custom-built experimental arrangement optimized for temperature-dependent studies. The setup comprised an Inel XRG3500 X-ray source (Cu anode, 45 kV,

10 mA), an Acton SpectraPro-500i monochromator, and a Hamamatsu R928 photomultiplier tube coupled to an APD Cryogenic closed-cycle helium cryostat. Spectra were collected over a temperature range from 300 K to 10 K in 10 K intervals. This controlled cooling sequence was implemented to minimize artifacts related to the thermal release of charge carriers, thereby enabling a reliable evaluation of the emission characteristics.

*PL and TRPL measurements*:
PL characterization was carried out using a picosecond 375 nm laser diode operated in continuous mode to excite the samples. The excitation and signal collection were performed through a microscope objective, ensuring precise optical alignment. The emitted PL was filtered with a 405 nm long-pass filter and recorded using a high-sensitivity fiber-coupled visible spectrometer. For TRPL measurements, the laser diode was operated in pulsed mode at a 10 MHz repetition rate. The emitted signal, passed through a 405 nm long-pass filter, was detected by a single-photon avalanche photodiode, and its temporal response was analyzed using time-correlated single-photon counting electronics (instrument response function, 0.3 ns). Temperature-dependent PL and TRPL measurements were performed using a Linkam HFS600E-PB4 cryostat equipped with a liquid-nitrogen cooling stage, allowing measurements between 80 K and 300 K in 10 K steps.

*Angle-resolved PL measurements*:
Angle-resolved PL measurements were carried out using a picosecond 405 nm laser diode operated in continuous-wave mode as the excitation source. The excitation beam was focused onto the sample surface, and the emitted signal was collected through a microscope objective. Residual excitation light was filtered using a 410 nm long-pass filter. The angle-dependent emission was coupled into an optical fiber and analyzed with a high-sensitivity fiber-coupled visible spectrometer. Six measurements were performed, and the resulting PL spectra were averaged.

*Quantum-optical modeling*:
The first-order coherence function $g^{(1)}(\tau)$ and the corresponding detected spectra were obtained using Python and the QuTiP quantum-optics library [48, 49]. A standard driven–dissipative two-level-system–cavity model was used, with all parameters (bare exciton and plasmon energies, linewidths, and coupling rate $g$) taken directly from experimental fits and FDTD-derived mode properties. The steady-state density matrix was calculated using `qutip.steadystate`. The two-time correlation function $\langle a^\dagger(t)a(t+\tau)\rangle$ was computed with `correlation_2op_1t`, and $g^{(1)}(\tau)$ was obtained by normalization. The detected spectra were generated via Fourier transformation of the correlation function following the Wiener–Khinchin relation. All simulations were performed without free parameters, using the same detuning and linewidth values extracted from the temperature-dependent RL and PL datasets.

*Uncertainty analysis*:
All uncertainties include both measurement variation and instrument-related contributions. Each value is based on three independent measurements, and the mean is reported. The statistical uncertainty is given by the standard deviation of these measurements. Uncertainties associated with detector accuracy, acquisition precision, and the fitting procedure are added in quadrature to this statistical term. For parameters obtained from spectral or temporal fits, the uncertainty corresponds to the fit standard error, combined with the instrumental contributions in the same way. This provides a consistent estimate of the total uncertainty for both measured quantities and fitted parameters. For derived quantities that depend on multiple fitted parameters, uncertainties were propagated using the total-differential method. This ensures a consistent estimate of the total uncertainty across both directly measured and calculated quantities.

**Supporting Information**
Supporting Information is available from the Wiley Online Library or from the author.

**Acknowledgements All authors** acknowledge research funds from the National Science Centre, Poland, under grant OPUS-24 no. 2022/47/B/ST5/01966. **M.M.** acknowledges the funds from the National Science Center, Poland, under grant Miniatura-8 no. 2024/08/X/ST5/00980 for consumable

purchase and his leave status from Nicolaus Copernicus University in Torun, Torun 87-100, Poland. **D.K.** acknowledges the funds from the National Science Center, Poland, under grant Miniatura-6 no. 2022/06/X/ST5/00369 for assembly of the angle-resolved PL setup.

## References

[1] S. van der Sar, S. Brunner, D. Schaart, *Med. Phys.* **2021**, *48*, 7 3708.

[2] C. Dujardin, A. Bessière, A.-L. Bulin, F. Chaput, B. Mahler, *Adv. Optical Mater.* **2025**.

[3] H. C. Delgado, P. Moradifar, G. Chinn, C. S. Levin, J. A. Dionne, *Nanophotonics* **2024**, *13* 1953.

[4] E. M. Purcell, *Phys. Rev.* **1946**, *69* 681.

[5] Y. Kurman, A. Shultzman, O. Segal, A. Pick, I. Kaminer, *Phys. Rev. Lett.* **2020**, *125* 040801.

[6] Y. Kurman, N. Lahav, R. Schuetz, A. Shultzman, C. Roques-Carmes, A. Lifshits, S. Zaken, T. Lenkiewicz, R. Strassberg, O. Beer, Y. Bekenstein, I. Kaminer, *Sci. Adv.* **2024**, *10*, 44 eadq6325.

[7] C. Roques-Carmes, N. Rivera, A. Ghorashi, S. E. Kooi, Y. Yang, Z. Lin, J. Beroz, A. Massuda, J. Sloan, N. Romeo, Y. Yu, J. D. Joannopoulos, I. Kaminer, S. G. Johnson, M. Soljacic, *Science* **2022**, *375* eabm9293.

[8] L. Martin-Monier, S. Pajovic, M. G. Abebe, J. Chen, S. Vaidya, S. Min, S. Choi, S. E. Kooi, B. Maes, J. Hu, M. Soljacic, C. Roques-Carmes, Large-scale self-assembled nanophotonic scintillators for x-ray imaging, **2025**.

[9] W. Ye, G. Bizarri, M. Birowosuto, L. Wong, *ACS Phot.* **2022**, *9*, 12 3917.

[10] W. Ye, Z. Yong, M. Go, D. Kowal, F. Maddalena, L. Tjahjana, H. Wang, A. Arramel, C. Dujardin, M. D. Birowosuto, L. J. Wong, *Adv. Mater.* **2024**, *36* 2309410.

[11] M. Makowski, W. Ye, D. Kowal, F. Maddalena, S. Mahato, Y. T. Amrillah, W. Zajac, M. E. Witkowski, K. J. Drozdowski, Nathaniel, C. Dang, J. Cybinska, W. Drozdowski, F. A. A. Nugroho, C. Dujardin, L. J. Wong, M. D. Birowosuto, *Adv. Mater.* **2025**, *37*, 30 e2417874.

[12] S. Noda, M. Fujita, T. Asano, *Nat. Photonics* **2007**, *1* 449.

[13] T. B. Hoang, G. M. Akselrod, M. H. Mikkelsen, *Nat. Commun.* **2015**, *6* 7788.

[14] A. Wibowo, M. D. Birowosuto, S. Gómez, R. P. Prasanna, et al., *Commun. Mater.* **2023**, *4*, 1 62.

[15] R. Kabe, C. Adachi, *Nature* **2017**, *550* 384.

[16] X. Ou, X. Qin, B. Huang, J. Zan, Q. Wu, Z. Hong, L. Xie, H. Bian, X. Chen, Y. Wu, X. Song, C. Le, Q. Chen, H. Yang, X. Liu, *Nature* **2021**, *590* 410.

[17] X. Li, J. Chen, D. Yang, X. Chen, D. Geng, L. Jiang, Y. Wu, C. Meng, H. Zeng, *Nat. Commun.* **2021**, *12* 3879.

[18] D. Kowal, S. Mahato, M. Makowski, S. Hartati, M. A. K. Sheikh, W. Ye, D. R. Schaart, J. Cybinska, L. J. Wong, A. Arramel, M. D. Birowosuto, *Appl. Phys. Rev.* **2025**, *12*, 1 011328.

[19] R. Chikkaraddy, B. de Nijs, F. Benz, S. J. Barrow, O. A. Scherman, E. Rosta, A. Demetriadou, P. Fox, O. Hess, J. J. Baumberg, *Nature* **2016**, *535* 127.

[20] S. Hu, J. Huang, R. Arul, A. Sánchez Iglesias, Y. Xiong, L. Liz-Marzán, J. Baumberg, *Nat. Commun.* **2024**, *15* 6835.

[21] P. Törmä, W. L. Barnes, *Rep. Prog. Phys.* **2015**, *78*, 1 013901.

[22] P. Y. Wen, C.-L. Zou, X. Guo, M.-J. Chien, J.-Y. Chen, T.-M. Chen, C.-Y. Sun, J. Li, Y. Wang, X. Li, T.-W. Lu, W. Y. Ching, D.-B. Tsai, H. X. Tang, *Nat. Photonics* **2016**, *10* 163.

[23] Q. Chen, J. Wu, X. Ou, B. Huang, J. Almutlaq, A. A. Zhukenekov, X. Guan, S. Han, L. Liang, Z. Yi, J. Li, X. Xie, Y. Wang, Y. Li, D. Fan, D. B. L. Teh, A. H. Al, O. F. Mohammed, O. M. Bakr, T. Wu, M. Bettinelli, H. Yang, W. Huang, X. Liu, *Nature* **2018**, *561* 88.

[24] M. Gandini, I. Villa, M. Beretta, C. Gotti, M. Imran, F. Carulli, E. Fantuzzi, M. Sassi, M. Zaffalon, C. Brofferio, L. Manna, L. Beverina, A. Vedda, M. Fasoli, L. Gironi, S. Brovelli, *Nat. Nanotechnol.* **2020**, *15* 462.

[25] G. Rainò, N. Yazdani, S. C. Boehme, M. Kober-Czerny, C. Zhu, F. Krieg, M. D. Rossell, R. Erni, V. Wood, I. Infante, M. V. Kovalenko, *Nat. Commun.* **2022**, *13* 2587.

[26] M. L. Zaffalon, F. Cova, M. Liu, A. Cemmi, I. Di Sarcina, F. Rossi, F. Carulli, A. Erroi, C. Rodà, J. Perego, A. Comotti, M. Fasoli, F. Meinardi, L. Li, A. Vedda, S. Brovelli, *Nat. Photon.* **2022**, *16* 860.

[27] J. Yu, S. Hou, M. Sharma, L. Y. M. Tobing, Z. Song, S. Delikanli, C. Hettiarachchi, D. Zhang, W. Fan, M. D. Birowosuto, H. Wang, H. V. Demir, C. Dang, *Matter* **2020**, *2* 1550.

[28] R. H. Dicke, *Phys. Rev.* **1954**, *93* 99.

[29] S. Hou, L. Y. M. Tobing, X. Wang, Z. Xie, J. Yu, J. Zhou, D. Zhang, C. Dang, P. Coquet, B. K. Tay, M. D. Birowosuto, E. H. T. Teo, H. Wang, *Adv. Opt. Mater.* **2019**, *7*, 22 1900857.

[30] P. Forn-Díaz, L. Lamata, E. Rico, J. Kono, E. Solano, *Rev. Mod. Phys.* **2019**, *91* 025005.

[31] M. Fu, P. Tamarat, J.-B. Trebbia, M. I. Bodnarchuk, M. V. Kovalenko, J. Even, B. Lounis, *Nano Lett.* **2018**, *18*, 2 815.

[32] M. J. Jurow, T. Morgenstern, C. Eisler, J. Kang, E. Penzo, M. Do, M. Engelmayer, W. T. Osowiecki, Y. Bekenstein, C. Tassone, L.-W. Wang, A. P. Alivisatos, W. Brütting, Y. Liu, *Nano Lett.* **2019**, *19*, 4 2489.

[33] C. Novo, A. M. Funston, P. Mulvaney, *Nat. Nanotechnol.* **2008**, *3*, 10 598.

[34] S. Babar, J. H. Weaver, *Appl. Opt.* **2015**, *54*, 3 477.

[35] J. Kang, L.-W. Wang, *Nano Lett.* **2018**, *18*, 2 705.

[36] A. Canales, T. Karmstrand, D. G. Baranov, T. J. Antosiewicz, T. O. Shegai, *Nanophotonics* **2023**, *12*, 21 4073.

[37] C. Zhu, T. Nguyen, S. C. Boehme, A. Moskalenko, D. N. Dirin, M. I. Bodnarchuk, C. Katan, J. Even, G. Rainò, M. V. Kovalenko, *Adv. Mater.* **2023**, *35*, 9 2208354.

[38] E. T. Jaynes, F. W. Cummings, *Proc. IEEE* **1963**, *51*, 1 89.

[39] G. Zengin, M. Wersäll, S. Nilsson, T. J. Antosiewicz, M. Käll, T. Shegai, *Phys. Rev. Lett.* **2015**, *114* 157401.

[40] A. Nirmal, S. Raja, A. S. Pawar, G. Konstantatos, E. H. Sargent, O. Millo, G. Haran, *Nat. Mater.* **2020**, *19* 1342.

[41] M. Balasubrahmaniyam, R. Saravanan, S. K. Sharma, P. A. Venkatesan, A. K. Sahu, A. A. Khan, A. K. Ghosh, P. K. Nayak, *ACS Nano* **2023**, *17*, 2 1423.

[42] A. Urban, L. Luber, D. Benedikt, A. Singldinger, *Research square* https://doi.org/10.21203/rs.3.rs–8603272/v1.

[43] X. Xu, S. Jin, Z. Zhen, J. Ren, *npj Nanophotn.* **2026**, *3*, 7.

[44] D. G. Lidzey, D. D. C. Bradley, A. Armitage, S. Walker, M. S. Skolnick, *Nature* **1998**, *395* 53.

[45] W. Shcherbakov-Wu, S. Saris, T. J. Sheehan, N. N. Wong, E. R. Powers, F. Krieg, M. V. Kovalenko, A. P. Willard, W. A. Tisdale, *Sci. Adv.* **2024**, *10*, 8 eadj6320.

[46] P. B. Johnson, R. W. Christy, *Phys. Rev. B* **1972**, *6* 4370.

[47] H. U. Yang, J. D'Archangel, M. L. Sundheimer, E. Tucker, G. D. Boreman, M. B. Raschke, *Phys. Rev. B* **2015**, *91* 235137.

[48] J. R. Johansson, P. D. Nation, F. Nori, *Comput. Phys. Commun.* **2012**, *183*, 8 1760.

[49] J. R. Johansson, P. D. Nation, F. Nori, *Comput. Phys. Commun.* **2013**, *184*, 4 1234.

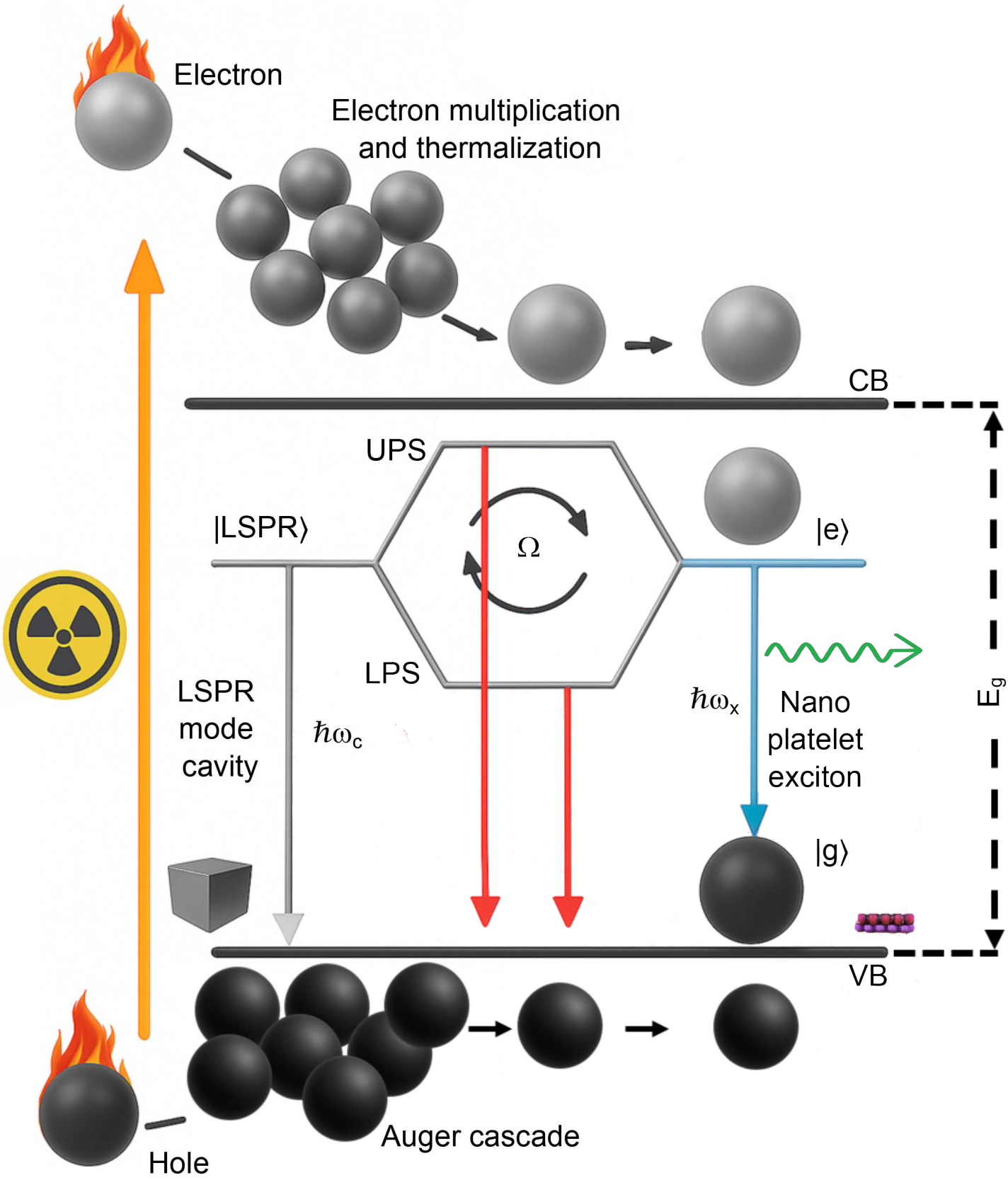


Figure 1: **Schematic overview of strong-coupling plasmonic scintillators.** Conceptual representation of exciton–plasmon interactions under ionizing-radiation excitation, leading to the formation of upper polariton states (UPS) and lower polariton states (LPS), separated by the Rabi splitting (Ω). The black and grey spheres denote holes and electrons, respectively, while the flame symbol marks the creation of hot carriers.

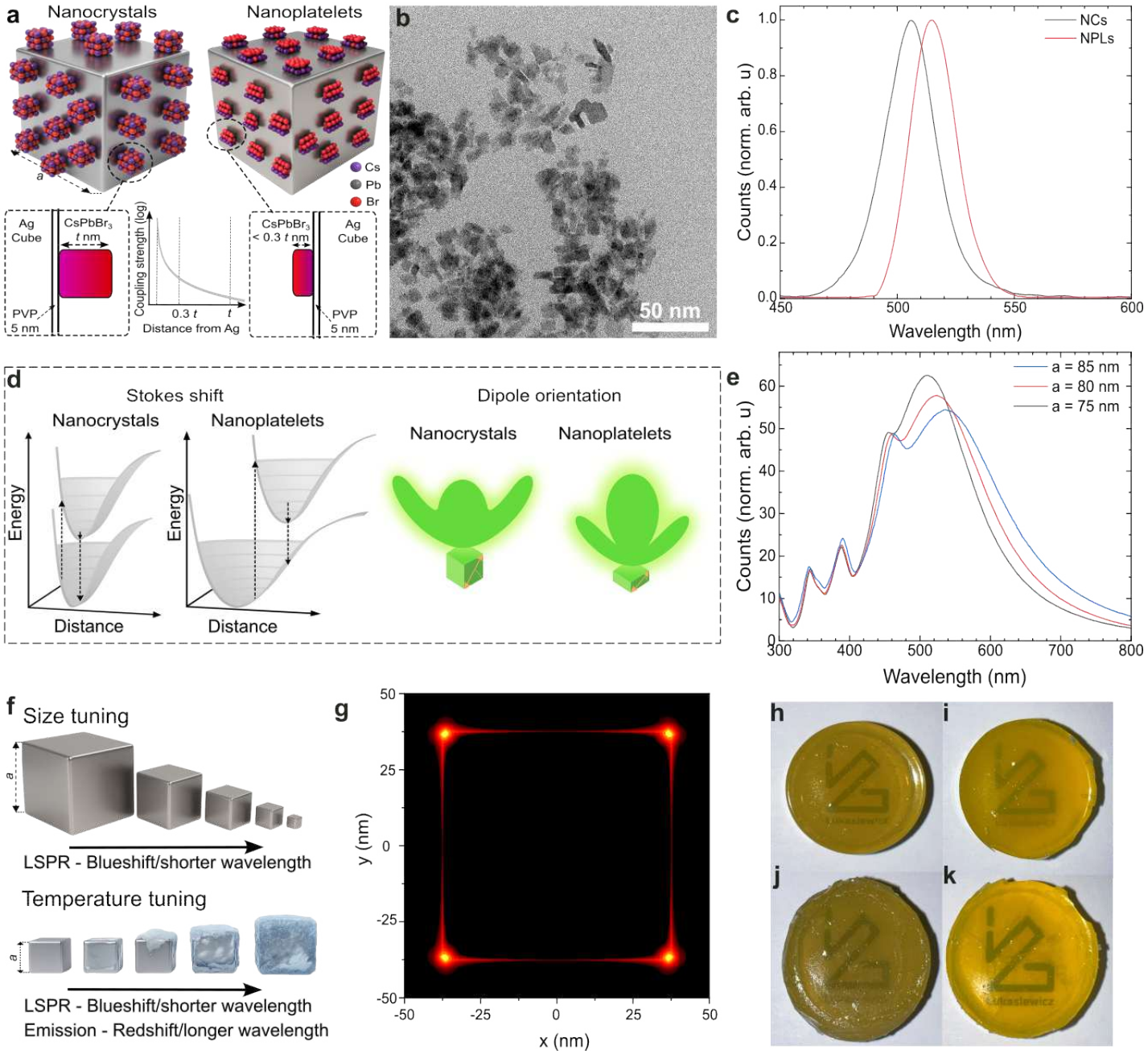


Figure 2: **Characterization and tuning of cesium lead bromide/silver ($CsPbBr_3$/Ag) composites. a**, Comparative summary between three-dimensional (3D) $CsPbBr_3$ nanocrystals (NCs) and two-dimensional (2D) $CsPbBr_3$ nanoplatelets (NPLs) deposited on silver cubic nanoparticles (Ag CNPs). Reducing the dimensionality from 3D to 2D decreases the average thickness ($t$) from (7.03 ± 0.20) to (1.93 ± 0.45) nm, thereby enhancing light–matter coupling. **b**, Transmission electron microscopy (TEM) image of $CsPbBr_3$ NPLs (white scale bar: 50 nm). **c**, Comparison of emission spectra between NCs and NPLs. **d**, Illustration of the larger Stokes shift and in-plane dipole orientation of NPLs compared with the isotropic dipoles of NCs, both favoring efficient coupling to radiative plasmonic modes. **e**, Measured scattering spectra of Ag nanocubes with side lengths ($a$) of 85, 80, and 75 nm. **f**, Optical tunability of the hybrid system achieved by adjusting the Ag CNP side length — causing a size-dependent blueshift of the localised surface plasmon resonance (LSPR) — and by varying the temperature, which induces an LSPR blueshift and an emission redshift, enabling spectral overlap at the zero-detuning temperature. **g**, Simulated local electric-field ($|E|$) distribution around an 80 nm Ag CNP under 520 nm in-plane dipole excitation, highlighting the field enhancement at the cube corners. **h**–**k**, Photographs of polydimethylsiloxane (PDMS)-based composites under ambient conditions: **h**–**j**, $CsPbBr_3$ NPL/Ag CNP composites with $a$ of 85 (**h**), 80 (**i**), and 75 (**j**) nm; **k**, $CsPbBr_3$ NPLs only.

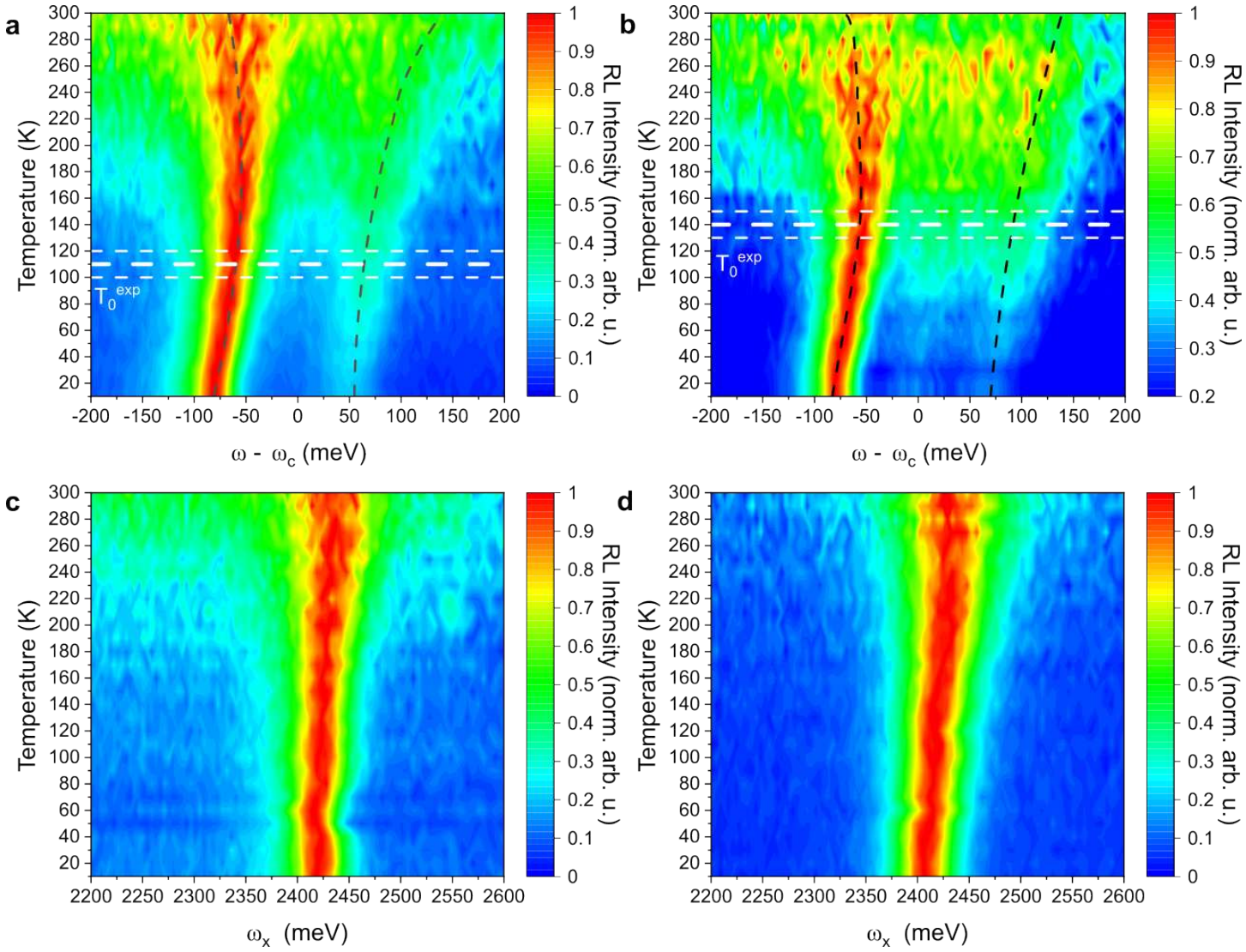


Figure 3: **Observation of polariton spectral splitting in $CsPbBr_3$/Ag composites under X-ray excitation.** **a–d**, Radioluminescence (RL) spectra measured over a temperature range of 10–300 K for composites containing Ag CNPs with side lengths of 85 (**a**), 80 (**b**), and 75 (**c**) nm, and for a reference sample without Ag (**d**). Black dashed lines in **(a)** and **(b)** serve as guides to the eye, indicating the formation of polariton branches, while the white dashed lines correspond with the experimentally derived zero detuning temperatures ($T_0^{exp}$) Spectra were shifted along the energy axis to align the polariton-splitting minima at the zero-detuning temperature (0 meV).

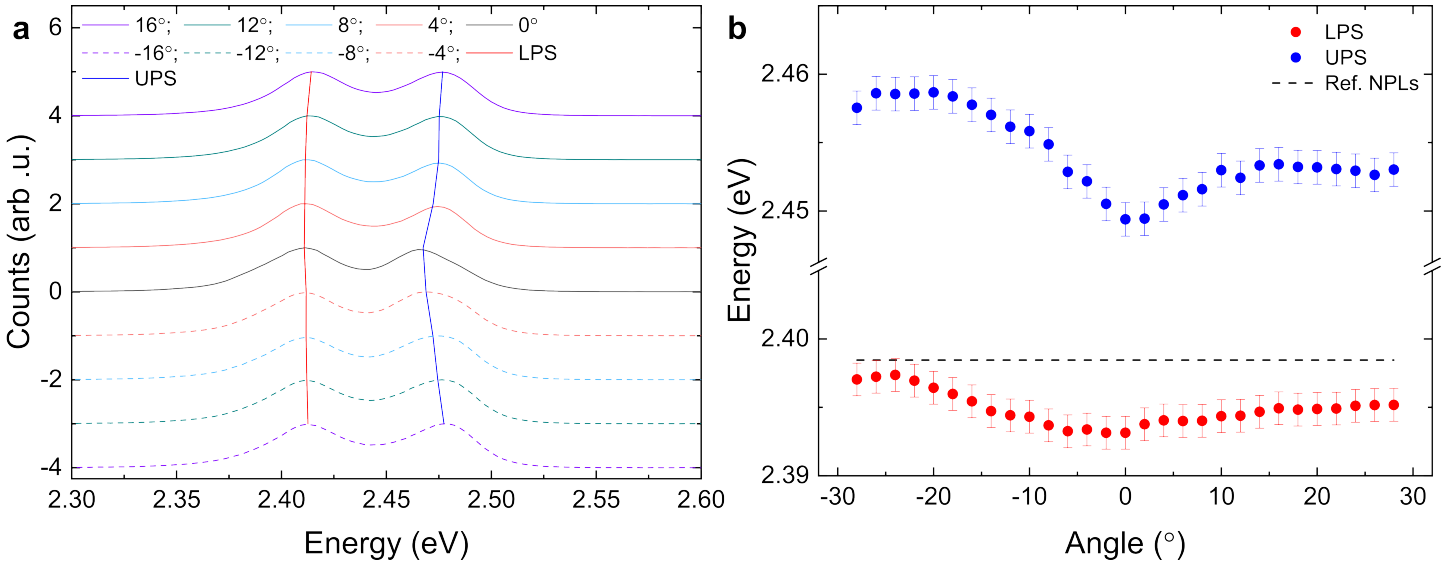


Figure 4: **Angle resolved analysis of polariton states formation under photoexcitation. a**, Comparison of PL spectra at various angles; the vertical lines eye-guide the position of each peak maximum. **b**. Polariton dispersion from angle-resolved PL spectra of $CsPbBr_3$ NPLs coupled with 80 nm Ag CNPs. Dashed black line corresponds to the position of reference sample emission maximum.

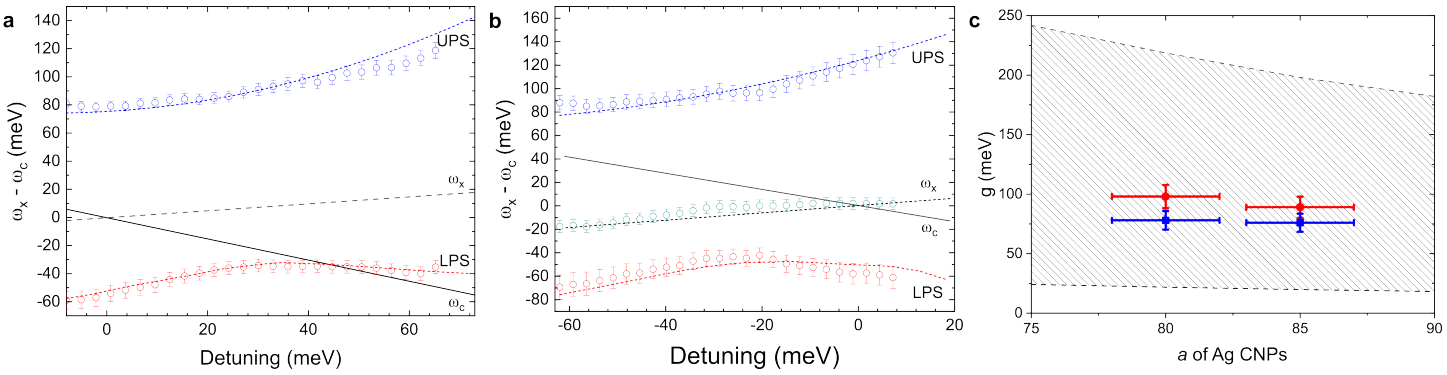


Figure 5: **Analysis of upper and lower polariton states and exciton-plasmon coupling rates. a,b**, Temperature-dependent evolution of plasmon–exciton polariton energies derived from RL spectra in Fig. 3. Polariton spectral splitting is plotted relative to the zero-detuning temperature ($\Delta = 0$ at 0 meV). Data correspond to Ag CNPs with side lengths of 85 nm (**a**) and 80 nm (**b**). Solid and dashed black lines represent the uncoupled emitter ($\omega_x$) and cavity ($\omega_c$) modes, respectively. Blue and red dashed lines denote the idealized UPS and LPS branches. Experimental points (symbols) correspond to maxima extracted from Lorentzian fits of the RL spectra. Additional green symbols in **b** indicate a third peak originating from the uncoupled emitter. **c**, Exciton-plasmon coupling rate as a function of Ag CNPs side length. Dashed area corresponds to the theoretical limits of $g$. Red and blue points correspond to the $g$ values extracted from the RL and PL measurements, respectively.

## Supplementary Files

This is a list of supplementary files associated with this preprint. Click to download.

- supporting.pdf